Taylor & Francis
Taylor & Francis Group

Image fluctuation model for damage detection using middle-resolution satellite imagery

M. KOHIYAMA*† and F. YAMAZAKI‡

†Department of System Design Engineering, Faculty of Science and Technology, Keio University, 3-14-1 Hiyoshi, Kohoku-ku, Yokohama 223-8522, Japan
‡Department of Urban Environment Systems, Faculty of Engineering, Chiba University, 1-33 Yayoicho, Inage-ku, Chiba 263-8522, Japan

A damage detection method using middle-resolution satellite images, the Image Fluctuation Model method, is proposed, which employs a stochastic model of the digital number (DN) fluctuation in a normal condition and its significance test. The DN fluctuation model is formulated by considering an imaging process of a satellite sensor and an image registration process. A resulting thematic map is created based on a confidence level (1−significance level), which is defined on a pixel-by-pixel basis as follows: the minimum significance level at which the null hypothesis, that the pixel DN can be considered as a sample of the DN fluctuation model, is rejected. The confidence level provides the model-based probability of ground surface change. The method is applied to the 2003 Bam, Iran earthquake using images acquired by Advanced Spaceborne Thermal Emission and Reflection Radiometer (ASTER) of Terra. The receiver operating characteristic curves of the method showed better detection performance than temporal image differencing or temporal image ratioing. Though the detection performance of building damage was not comparable to visual inspection on a building basis using high-resolution images of QuickBird, the confidence level map shows similarity at the district level to damage assessment results using high-resolution images.

1. Introduction

Although high-resolution satellite imagery has received much attention due to its imaging capability, middle-resolution satellite imagery for which the ground sampling interval is larger than 10 m should also be utilized for damage detection. This is for the following reasons: (1) its wider swath can depict the perspective view of wide-ranging disaster areas; (2) its ample archive of previously acquired images can provide pre-event images for almost any location after a disaster. In addition, the cost of an image per area is considerably lower than that of a high-resolution image. It is commonly accepted practice for all available information to be used for disaster relief activities. Thus, we have to promote research in the area of damage detection methods using middle-resolution imagery as well as higher-resolution imagery.

Many researchers have proposed change detection procedures: comparison of land cover classifications, multi-date classification, image differencing/ratioing, index differencing (e.g. vegetation index, tasselled-cap indices), principal components analysis and change vector analysis (Singh 1989, Lu *et al.* 2004). In the final

---

*Corresponding author. Email: kohiyama@sd.keio.ac.jp

stage of most techniques, change and no change may be judged by a simple thresholding as a '0–1' binary response:

$$change(x, y) = \begin{cases} 0 & (f(\mathbf{Q}) \leq T) \\ 1 & (f(\mathbf{Q}) > T) \end{cases} \qquad (1)$$

where x and y represent the location of interest on the ground, the vector $\mathbf{Q}$ represents digital numbers (DNs) of satellite images ($\mathbf{Q}$ can also represent multi-band and/or multi-temporal data) and T is the threshold value provided statistically or empirically by the analyst. There are many criteria used in order to determine the threshold. These are based on two probability density functions with respect to $\mathbf{Q}$ corresponding to two hypotheses that change does occur and that change does not occur: e.g. Bayes criterion, maximum *a posteriori* (MAP) detection, maximum likelihood criterion (ML), minimum error probability criterion, minimax criterion, Neyman–Pearson criterion (Van Trees 1968, Kazakos and Papantoni-Kazakos 1990, Poor 1994, McDonough and Whalen 1995, Helstrom 1995, Hippenstiel 2002). Once threshold values are introduced, the change in categorical attributes of the target areas can be evaluated, e.g. from forest to urban, from no change to change.

In the case of damage detection, however, it is a difficult task to determine a threshold value discriminating damage and no damage after a severe disaster because we often face the lack of prior reference data of damage areas (images containing damage), i.e. it is difficult to obtain the probability density function corresponding to a hypothesis that change does occur. In addition, a threshold value derived from few reference data is unreliable; moreover, a threshold value may change from region to region and from country to country. This is because the inherent variety of urban structures implies that a certain threshold may not be valid for a different city any longer.

By giving up using a threshold of a binary response, the damage detection result can be depicted in a map with colours or grey levels based on magnitude of a certain measure of change, such as DN difference. With respect to this measure of change, probabilistic expression, e.g. probability of damage occurrence, makes it much easier for an analyst to interpret the result map than difference in DN or change of reflectance. Hence, probabilistic expression of damage occurrence rather than a binary response result can alleviate the difficulty associated with the uncertainty and arbitrariness of threshold values and has the added advantage that an image interpreter can easily understand the credibility of the evaluation result.

Morisette *et al.* (1999) proposed the use of generalized linear models (GLMs) in change detection and the generation of a thematic map of 'probability of (category) change'. However, GLMs such as logit and probit models require sample reference data in a regression analysis, and deficiency of reference images of earthquake damage and the above-mentioned regional differences hinder the employment of GLMs. Hence, a new approach is necessary to overcome these problems. Kohiyama *et al.* (2004) proposed a method to estimate disaster-afflicted areas based on night-time images acquired by the Defense Meteorological Satellite Program Operational Linescan System (DMSP-OLS). That approach used significance levels (confidence levels) in a thematic map based on a probability density function of radiance of urban city lights, which are derived from multiple pre-event images; i.e. a probability density function corresponding to the hypothesis that change does not occur is solely used.

This paper provides a theoretical framework to the method of Kohiyama *et al.* (2004) for non-sensor-specific images (either daytime or night-time) that are

acquired by a middle- or low-resolution sensor on a satellite and proposes a new damage (change) detection method, introducing a probability model of DN fluctuation in an image pixel and its significance test. The method overcomes uncertainty, arbitrariness, and difficulty of threshold setting in conventional change detection methods.

2. Damage detection method based on a probability model of digital numbers in multi-temporal images

2.1 *Digital number of middle-resolution image as a random variable*

Our proposed method to detect damage is based on the principle that the DN of a fixed point (location on the ground) can be considered as a random variable. DNs of remotely sensed images change and fluctuate even in a normal (non-disaster) situation. This section explains how DN can be modelled as a random variable based on the overall sensor model of an electro-optical remote sensing system (Schowengerdt 1997).

In the scanning operation of a satellite sensor, the radiance of band b, s_b, is converted into the electric signal, e_b:

$$e_b(x, y) = \int\int s_b(\alpha, \beta) PSF(x - \alpha, y - \beta)\, \mathrm{d}\alpha\, \mathrm{d}\beta \qquad (2)$$

where *PSF* is the point spread function (PSF) of the whole sensor system, and α and β are parameters for spatial integration; e.g. α in the cross-track direction and β in the along-track direction. The function *PSF* of equation (2) includes an optical process. As an example, the PSF of the Advanced Spaceborne Thermal Emission and Reflection Radiometer (ASTER) of Terra is shown in figure 1. The shape of the PSF is estimated based on the measured values of the modulation transfer function at the Nyquist and the 1/2 Nyquist spatial frequencies for the along-track and cross-
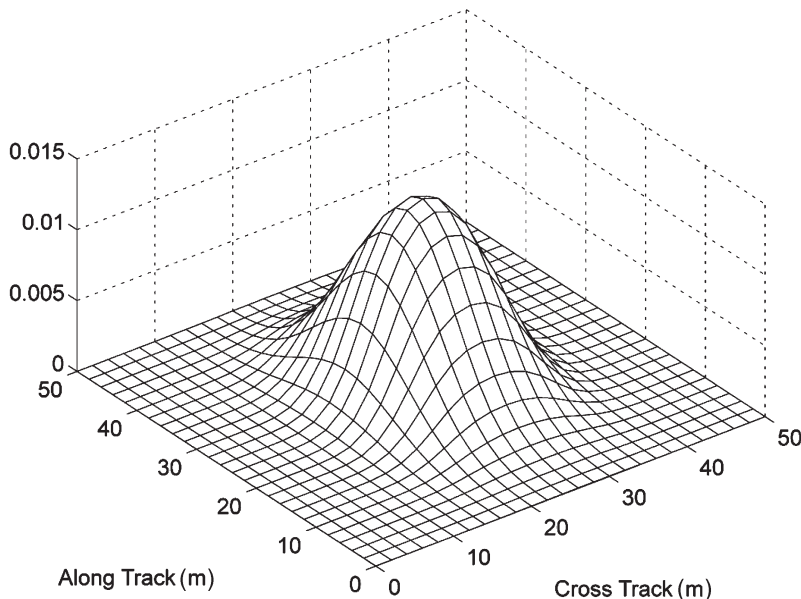

Figure 1. Estimated point spread function of VNIR radiometer subsystem of Terra-ASTER.

track directions with the specified values with respect to the visible–near infrared (VNIR) radiometer subsystem (Earth Remote Sensing Data Analysis Center 2001).

The analog-to-digital (A/D) converter samples and quantizes the electric signal into discrete DN values, $P(x, y)$:

$$P(x, y) = \text{int}(gain_b \times e_b(x, y) + offset_b) \tag{3}$$

where $gain_b$ and $offset_b$ represent the parameters of the linear A/D conversion.

These equations implicitly include the conversion from a continuous spatial coordinate to a discrete one. Usually, the discrete coordinates are different among images, and there exists a difference of the *sample-scene phase*, or pixel centre offset, that is the relative location of the pixels and the target. The relative spatial phase is unpredictable and typically unknown for any given image acquisition. We assume it follows the two-dimensional uniform probability distribution between $\pm 1/2$ pixels for the cross-track and along-track directions.

In an analysis using multi-temporal images, all the images are registered and the offsets are adjusted to the single reference image. The bilinear interpolation or the cubic convolution is typically used in registration, and these interpolation processes are expressed as:

$$Q(x, y) = \text{int}\left(\begin{bmatrix} 1-t & -t \end{bmatrix} \begin{bmatrix} P_{11} & P_{12} \\ P_{21} & P_{22} \end{bmatrix} \begin{bmatrix} 1-s \\ -s \end{bmatrix} \right) \text{ for bilinear interpolation} \tag{4}$$

$$Q(x, y) = \text{int}\left(\begin{bmatrix} S(1+t) & S(t) & S(1-t) & S(2-t) \end{bmatrix} \begin{bmatrix} P_{11} & P_{12} & P_{13} & P_{14} \\ P_{21} & P_{22} & P_{23} & P_{24} \\ P_{31} & P_{32} & P_{33} & P_{34} \\ P_{41} & P_{42} & P_{43} & P_{44} \end{bmatrix} \begin{bmatrix} S(1+s) \\ S(s) \\ S(1-s) \\ S(2-s) \end{bmatrix} \right)$$

$$S(t) = \begin{cases} (\alpha_{PCC} + 2)|t|^3 - (\alpha_{PCC} + 3)|t|^2 + 1 & (|t| < 1) \\ \alpha_{PCC}(|t|^3 - 5|t|^2 + 8|t| - 4) & (1 \le |t| < 2) \\ 0 & (|t| \ge 2) \end{cases} \tag{5a, b}$$

$$\left(\approx \text{sinc}(t) = \frac{\sin \pi t}{\pi t} \right) \text{ for cubic convolution}$$

where the $Q(x, y)$ is an integer DN of the registered image, the vector (x, y) is the location in the adjusted coordinate system, P_{ij} represents DNs of the 4 or 16 points surrounding the point (x, y) as shown in figure 2. The parameter $\alpha_{PCC} = -0.5$ is used as an optimal value (Keys 1981, Park and Schowengerdt 1983, Schowengerdt 1997). The vector (s, t) represents the phase of two directions with each element ranging from 0 to 1 (figure 2), and this is a random variable following the two-dimensional uniform probability distribution, as we assumed. Therefore, by assuming there is no quantization error in equation (3), the DN of the registered image, $Q(x, y)$, is:

$$Q(x, y) \approx \text{int}\left(gain_b \iint s_b(\alpha, \beta) SPSF(x-\alpha, y-\beta)\, d\alpha\, d\beta + offset_b \right)$$

$$SPSF(x, y) = \sum_{i=1}^{n} \sum_{j=1}^{n} W_{ij} PSF(x - x_{ij}, y - y_{ij}) \tag{6a, b}$$

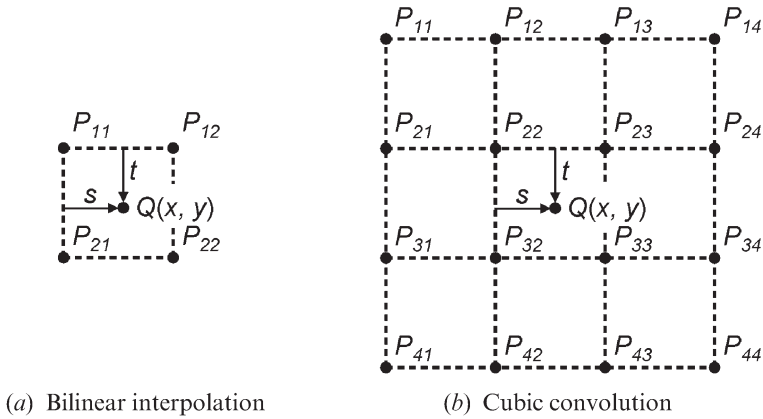(*a*) Bilinear interpolation   (*b*) Cubic convolution

Figure 2. A point to be registered with a digital number of $Q(x, y)$, and points used in registration with digital numbers of P_{ij} based on (*a*) the bilinear interpolation and (*b*) the cubic convolution. Note that parameters s and t range $[0, 1)$ to indicate the location of a point to be registered, (x, y).

and

$$[W_{ij}] = \begin{bmatrix} 1-t \\ -t \end{bmatrix} [1-s \quad -s] \text{ for bilinear interpolation } (n=2) \tag{7}$$

$$[W_{ij}] = \begin{bmatrix} S(1+t) \\ S(t) \\ S(1-t) \\ S(2-t) \end{bmatrix} [S(1+s) \ S(s) \ S(1-s) \ S(2-s)] \text{ for cubic convolution } (n=4) \tag{8}$$

where the vectors (x_{ij}, y_{ij}) $(i=1, 2, \ldots, 4$ and $j=1, 2, \ldots, 4)$ represent the pixel centre locations of the surrounding 16 points. The equations (6a, b), (7) and (8) describe the DN of a pixel as a random variable. Thus, the DN of the same target varies from acquisition to acquisition even in a normal, non-disaster condition.

Registration errors always remain even if sub-pixel accuracy is achieved in registration. This has the effect of increasing the randomness of the DNs. Obviously, there exist other well-known factors that increase the randomness: electronic noise in a sensor system, atmospheric correction error, solar position difference (shade, shadow, etc.), phenological change, soil moisture differences, relative ground sampling interval changing along the off-nadir scan angle, etc. The quantization error in equation (3), which we assumed to be negligible in the formulation, is also one of the factors.

2.2 *Modelling of probability distribution of digital numbers*

As formulated in the previous section, the DN of each location can be modelled as a random variable. Equations (6a, b) and the two-dimensional uniform distribution of the variables s and t can be employed in evaluating the probability distribution of DN. Alternatively multi-temporal images serve as sample data to evaluate the probability distribution. Although the number of pre-event images may be limited, collecting these images is much easier than conventional approaches of change

detections: gathering reference images of earthquake damage for training data and considering regional differences between the reference and target areas.

The DN fluctuation model for some categorized urban areas is an optional solution to increase the sample data, but it may result in decreased change detection accuracy because pixels with different probability distributions are involved and the variance of the categorized model is clearly larger than that of a single pixel model.

2.3 *Damage or change detection based on a significance test*

Suppose that the DN or the fluctuation of DN is given as the probability distribution $Pr(Q)$, where Q represents a DN in an image acquired at a non-eventful time, i.e. before a disaster. Now, we introduce the following null hypothesis:

> Null hypothesis H_0: When the digital number, $q(x, y)$, of the location (x, y) on the ground is acquired, $q(x, y)$ is considered as a sample of the probability distribution, $Pr(Q)$.

A significance test is made based on a significance level of α. If q is in a range of small fluctuation and H_0 cannot be rejected, we have no choice but to accept there is no change on the ground. But, if H_0 is rejected, we can judge that there exists an abnormal change on the ground which exceeds the fluctuation level at a non-eventful time, i.e. possible damage. Therefore, considering the significance test for each location, a significance level, $\alpha(x, y)$, which satisfies the following equation can be evaluated on a pixel-by-pixel basis:

$$1 - \alpha = \int_{q_1}^{q_2} pr(Q) \, \mathrm{d}Q \tag{9}$$

where $pr(Q)$ is a probability density function of $Pr(Q)$ and the integration range, $[q_1, q_2]$, is given by $pr(q_1) = pr(q_2) = pr(q)$ and $q_1 < q_2$ as in a two-sided test. Figure 3 depicts the evaluation of confidence level, $1 - \alpha$, which is given by integration of the probability density between q_1 and q_2. The confidence level, $1 - \alpha$, means that the observed DN, q, is considered to be abnormal (a change or damage occurs there)
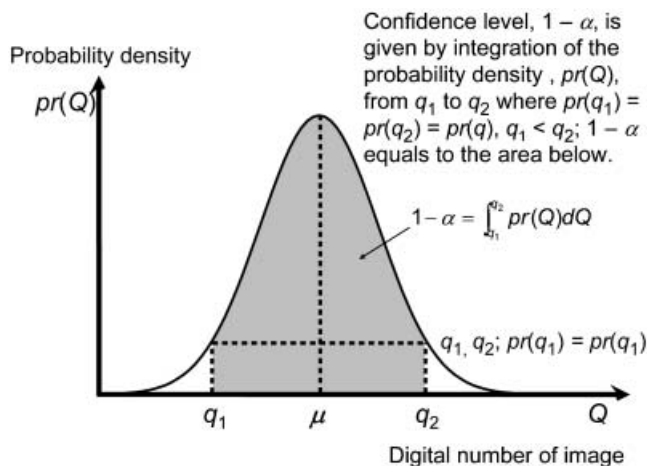

Figure 3. Evaluation of confidence level, $1 - \alpha$. In this example, q, which is a digital number acquired after a disaster, includes a change (damage) with confidence level $1 - \alpha$.

with this probability. Note that $Pr(Q)$ can be any probability distribution other than the normal (Gaussian) distribution.

As previously mentioned, the DN fluctuation model for some categorized urban areas is an alternative way to increase the sample data, but it may result in decreased change detection accuracy because pixels following different probability distributions are involved and the variance of the categorized model is clearly larger than that of a single pixel model.

Finally, the map of credibility (probability) of damage occurrence will be obtained by mapping the distribution of the confidence level, $1-\alpha$, or the significance level, α.

2.4 *Flow of damage detection*

Figure 4 shows the flow chart of our proposed method, the Image Fluctuation Model (IFM) method to detect damage (change) using middle-resolution imagery acquired by a satellite sensor:

- Step 1: Collect the multi-temporal pre-event images.
- Step 2: Register these images and compensate for radiometric and atmospheric effects.
- Step 3: Evaluate a probability distribution, $Pr(Q)$, for each DN using the above processed images.
- Step 4: Acquire a post-event image.
- Step 5: Register the post-event image and compensate for radiometric and atmospheric effects.
- Step 6: Evaluate the significance level, α, or the confidence level, $1-\alpha$, on a pixel-by-pixel basis for each pixel in a target area using each probability model, $Pr(Q)$, so that the null hypothesis, that the DN is a sample of $Pr(Q)$, can be rejected with the significance level α.
- Step 7: Create a thematic map of confidence level, $1-\alpha$, to depict the damage (change) probability of each pixel.
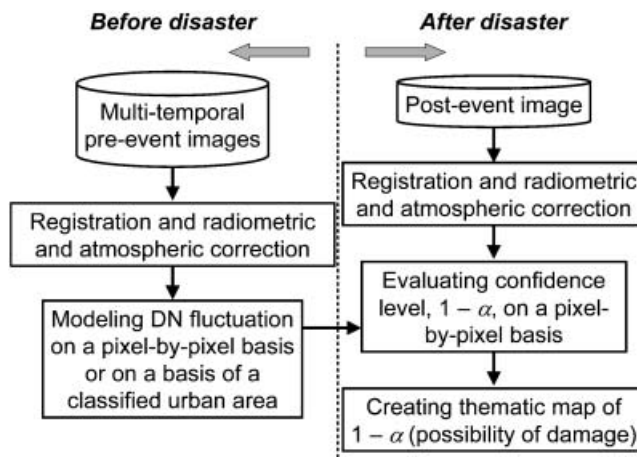

Figure 4.   Flowchart of the Image Fluctuation Model (IFM) method. For pre-event images, registration and correction of radiometric and atmospheric effects, which might be very time-consuming, can be done in advance before occurrence of a severe disaster if these processes are implemented in an image archiving system.

The bottleneck of the processing time exists in precise registration and in compensation of radiometric and atmospheric effects of images. However, these processes for pre-event images can be carried out in advance if they are implemented in an image archiving system.

2.5 *Images applicable to the Image Fluctuation Model*

Considering the source of the randomness of DN comes from the uncertainty of a sample-scene phase, any other images derived from satellite imagery theoretically imply the same randomness. In other words, any value of raw band data, index (e.g. normalized difference vegetation index) or principal component can be the input variable, Q, in equation (4) or (5a, b).

In addition, it is a simple matter to expand the dimension of Q and $Pr(Q)$ into a higher order by using a multi-dimensional probability distribution. This is done in order to apply them to multi-band imagery. Figure 5 describes evaluation of confidence level, $1-\alpha$, in the case that the input variable is two-dimensional, i.e. $\mathbf{Q}=(Q_1, Q_2)$. In the upper left side of the figure, an oblique view of a probability density surface, $Pr(Q_1, Q_2)$, is shown where Q_1 and Q_2 are two independent digital numbers of a satellite image. When a datum $\mathbf{q}$ is observed, the iso-probability-density line (contour line) including the point $\mathbf{q}$ can be defined as shown in the vertical view in the lower left of the figure; this contour line bounds the integration region A. The confidence level, $1-\alpha$, is given by integration of the probability density in the region A. The confidence level, $1-\alpha$, is equal to the volume of the object that is bounded by the probability density surface, the Q_1Q_2-plane, and the surface made by the above-mentioned contour line moving to the $Pr(Q_1, Q_2)$ direction.

Probability density
$pr(Q_1, Q_2)$

Q_1

Digital number of Band m

Digital number of Band n

Observed data $\mathbf{q}$ Q_2 (Oblique view)

Confidence level, $1-\alpha$, is given by integration of the probability density in the region A; $1-\alpha$ equals to the volume of the above object.

Digital number of Band m, Q_1

Integration region A

Digital number of Band n

Q_2 Observed data $\mathbf{q}$

$$1-\alpha = \iint_A pr(Q_1, Q_2) dQ_1 dQ_2$$

Iso-probability-density line (contour line) that includes the observed data $\mathbf{q}$; the integration region A is bounded by this line.
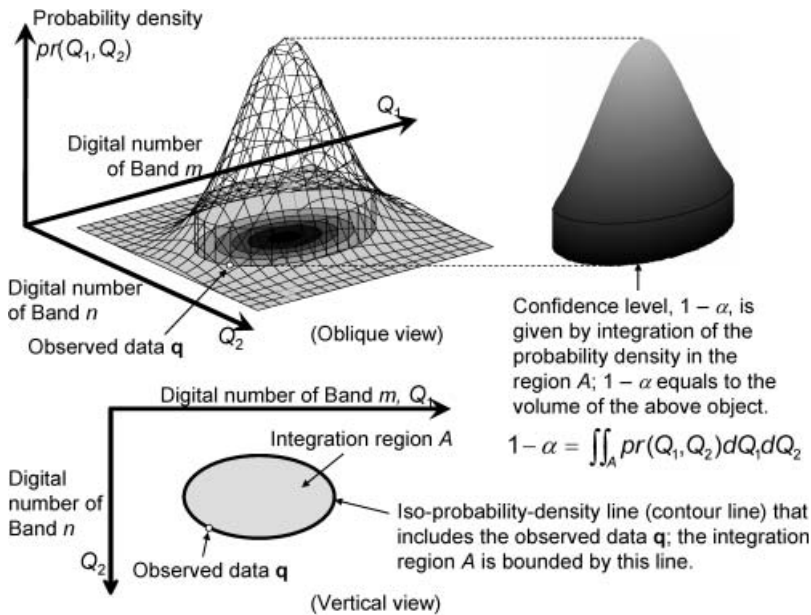
(Vertical view)

Figure 5. Evaluation of confidence level, $1-\alpha$, when the fluctuation model of digital

If the DN fluctuation model is assumed as a multi-dimensional Gaussian distribution, a contour surface of the probability density becomes a hyper-ellipsoid (figure 6). In this case, the confidence level, $1-\alpha$, is given by integration of the probability density in the region V that is bounded by the contour surface including an observed datum $\mathbf{q}$. This hyper-ellipsoid seems to be similar to the Ellipsoidal Change Detection (ECD) method proposed by Dai and Khorram (1998), which employs a Gaussian distribution and the Mahalanobis distance function of an n-dimensional difference image. But the IFM method differs substantially from the ECD method; the former method does not require threshold setting whereas the latter method does. The resulting thematic map of the IFM method shows the confidence level (or significance level) of each pixel area and it reflects the credibility of the possible damaged area.

3. Application to the 2003 Bam, Iran earthquake

3.1 *2003 Bam, Iran earthquake*

The 2003 Bam, Iran earthquake devastated Bam City in Kerman province. Eshghi and Zare (2003) reported that the Bam earthquake of 26 December 2003 (M_w=6.5) occurred at 01:56:56 UTC (05:26:26 local time) around Bam City in south-east Iran.

According to the United Nations, Office for the Coordination of Humanitarian Affairs (UN-OCHA 2004a) as of 17 March 2004, the updated assessment of the impact of the earthquake, as provided by the Government of Iran, indicates that there were approximately 43 200 people dead, 15 000 still under medical treatment, 2000 orphaned and up to 90 000 people displaced. This was in addition to the destruction of 50 000 houses in Bam and the surrounding rural areas. The number of people affected by loss of economic activity and damage to property and infrastructure was up to 200 000. Because the earthquake struck at a time when most residents were sleeping, it had a great impact on number of lives lost. In contrast to the aforementioned reported statistics, Iran's statistics office announced
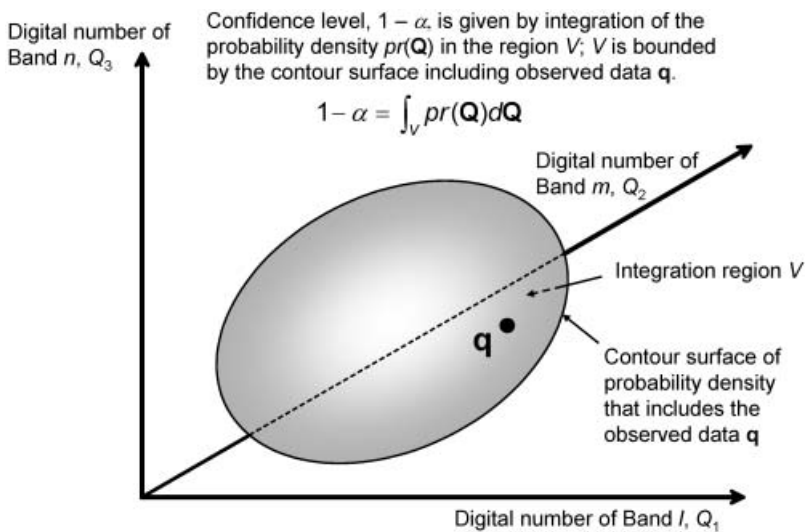

Figure 6. Evaluation of confidence level, $1-\alpha$, when the fluctuation model of digital numbers is expanded into a multi-dimensional probability distribution.

that the death toll in Bam City was 26 271 as of 30 March 2004 (United Nations Office for the Coordination of Humanitarian Affairs, 2004b).

3.2 *Satellite images used in the study*

For damage detection due to this earthquake in Bam City, satellite images acquired by Terra-ASTER were employed, of which the ground sampling distance was 15 m for the three nadir-looking bands and one backward-looking band of the VNIR radiometer (Yamaguchi *et al.* 1998, Abrams 2000). Table 1 shows the spectral bands and the looking directions of VNIR radiometer of Terra-ASTER. In this case study, 17 pre-event images and one post-event image of the product Level 1B (radiance registered at sensor) were used. One exception, an image of 23 February 2003 (2003-02-23), is listed in table 2. With respect to the 2003-02-23 image (referred to the master image), the product Level 2B05V (surface reflectance) was used as a master reference image in registration and histogram matching in order to adjust the DN scale to reflectance. In generating the product Level 2B05V, data provided by US National Centers for Environmental Prediction (NCEP) was used for sources of water vapour profile, temperature profile and pressure profile. Climatological estimates were used for other sources of aerosol, ozone, carbon dioxide, etc. In the master image, Bam City was acquired in the centre of a swath (nadir from the satellite) rather than in an edge part. Note that the 18 images were selected since they had very few or no clouds above Bam City. When the sun elevation, earth–sun distance, and topographic and atmospheric effects are considered, it seems that the product level of surface reflectance should be used for all the images. However, if the product level of surface reflectance was used for all the images, the result of the confidence levels became significantly large for most of the pixels in the post-event image; this is possibly due to soil moisture change because there was precipitation a few days before the post-event image acquisition and the signal-to-noise ratio of change detection clearly increased. Thus, this study focused on the change in relative

Table 1. Spectral bands and looking directions of VNIR radiometer of Terra-ASTER.

Band name	Spectral range (wavelength range, μm)	Looking direction
Band 1	0.52–0.60	Nadir
Band 2	0.63–0.69	Nadir
Band 3	0.76–0.86	Nadir
Stereoscopic band*	0.76–0.86	Backward

*Not used in the study.

Table 2. Acquisition dates of Terra-ASTER images of Bam City used in the study.

Period	No. of images	Acquisition date (year-month-day)
Pre-event	17	2000-07-15, 2001-05-15, 2001-06-09, 2001-07-11, 2001-07-27, 2001-11-16, 2002-03-08, 2002-03-15, 2002-04-16, 2002-06-19, 2002-10-25, 2002-11-10, 2003-02-07, 2003-02-23*, 2003-05-05, 2003-08-09, 2003-10-28
Post-event	1	2004-01-02

*For the 2003-02-23 image, Level 2B05V product (surface reflectance) was used as a master image in registration; for the others, Level 1B images (radiance registered at sensor) were used.

spatial pattern rather than the absolute reflectance change in urban areas for each spectral band. From a practical standpoint, the sun elevation, earth–sun distance, and topographic and atmospheric effects were simply excluded by histogram matching of DNs with respect to pixels in the urban areas of Bam City. In selection of pixels in the urban areas, the normalized difference vegetation index (NDVI), (Band 3−Band 2)/(Band 3+Band 2) where Band n means a digital number of ASTER Band n, was used for the master image, and the criterion NDVI less than 0.3 was adopted as shown in figure 7. In this city, the vegetation areas, which have large NDVI, consist mostly of date palm plantation farms. It should be noted that the months of the acquisition dates of the pre-event images are distributed evenly throughout a year, and thus seasonal change is included in the models of DN fluctuation. Therefore, this bias would reduce the signal-to-noise ratio in damage detection.

3.3 *Modelling of digital number fluctuation*

3.3.1 Registration of pre-event images. First, image registration was carried out with respect to the 17 pre-event images. Some of the pre-event images do not cover the entire urban area of Bam City and the number of pre-event images at each location is shown in figure 8, in which the grey near-vertical stripes overlaying the city image show the areas that have the same number of pre-event images. The numbers of pre-event images are noted both above and below the stripes. Fifty ground control points (GCPs) (30 GCPs for the 2002-03-15, 2002-04-16 and 2002-11-10 images due to the narrower coverage) were selected from the intersections of roads in the master image of 2003-02-23. The locations of GCPs in an image to be registered (referred to as a slave image) were sought with accuracy up to a tenth of pixel size (i.e. 1.5 m) with iterative analysis so that the locations give the maximum image correlation with the master image. Note that Dai and Khorram (1998) showed that highly accurate change detection based on multi-temporal Landsat
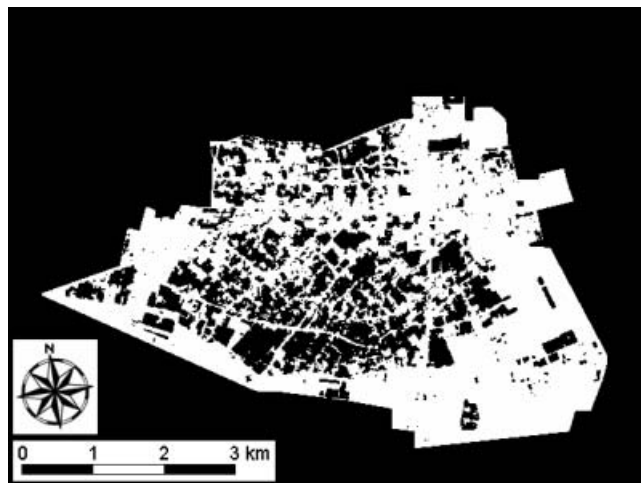

Figure 7. Pixels used for histogram matching (shown in white), which are derived from the urban areas of Bam City, and those pixels with a normalized difference vegetation index, (Band 3−Band 2)/(Band 3+Band 2), less than 0.3 for the 2003-02-23 master image (Band n means a digital number of ASTER Band n).
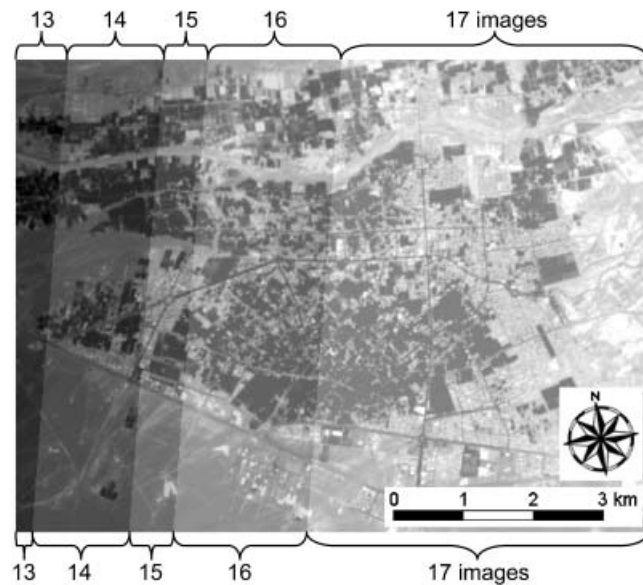
Figure 8. Numbers of pre-event images covering Bam City; the grey near-vertical stripes overlaying the city image show the areas that have the same number of pre-event images; the numbers of pre-event images are shown both above and below the stripes.

Thematic Mapper images requires that the magnitude of misregistration be less than 0.2 pixels. Since slight band-to-band misregistration is observed in VNIR images of Terra-ASTER, especially in the images in which Bam City was acquired in the edge part of the swath rather than the centre, registration was carried out band by band. Note that ERSDAC (2001) describes the baseline performance requirements of in intra-telescope registration accuracy as 0.2 pixels, which suggests that precise change detection using multi-band images requires the re-registration of the images even though the images were acquired by the same telescope system simultaneously. In evaluation of image correlation, a window size of 51×51 was used considering skew and rotation of a slave image based on the GCPs of the previous step in the iterative analysis and a histogram of DNs in a window of a slave image matched to that of the master image. Based on 50 pairs of the identified GCPs (or 30 pairs for the above-mentioned three images), the 16 slave images were registered by using a warping method of the bilinear interpolation. The bilinear interpolation method is expected to result in a smaller influence of a significantly changed DN on the surrounding pixels than the cubic convolution method since a smaller number (4) of surrounding pixels is used rather than a larger number (16) as shown in figure 2.

3.3.2 Histogram matching of digital numbers. After registration, the DNs of the pre-event images were linearly transformed on a band basis so that the average and the standard deviation of DNs of the pixels in urban areas shown in figure 7 may become identical to those of the master image. Figures 9 and 10 show the pre-event 2003-02-23 image (the master image) of the product Level 2B05V, and the post-event 2004-01-02 image, which was registered and histogram-matched from the product Level 1B to the master image, respectively. In these images, red, green and blue represent ASTER Bands 3, 2 and 1, respectively.
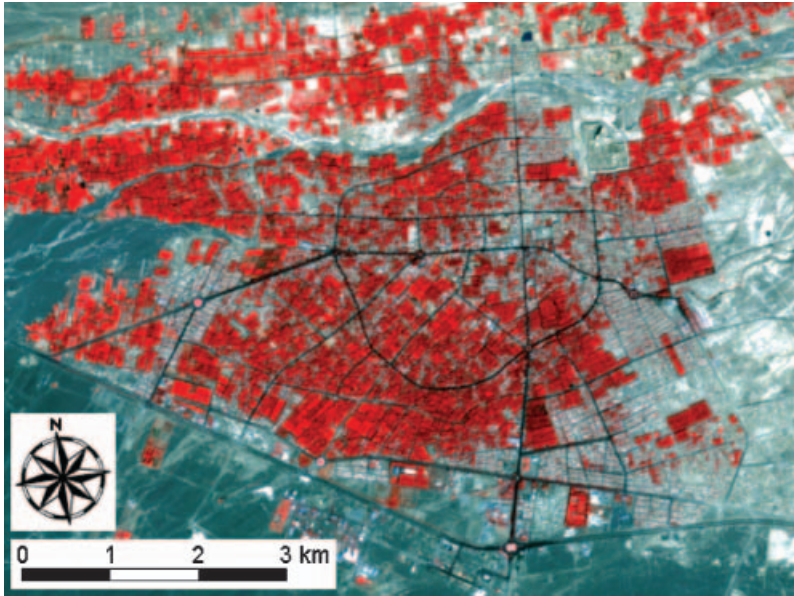
Figure 9. Pre-event image of Bam City acquired on 23 February 2003; red, green and blue correspond to ASTER Bands 3, 2 and 1, respectively. The product level of surface radiance (Level 2B05V) was used.
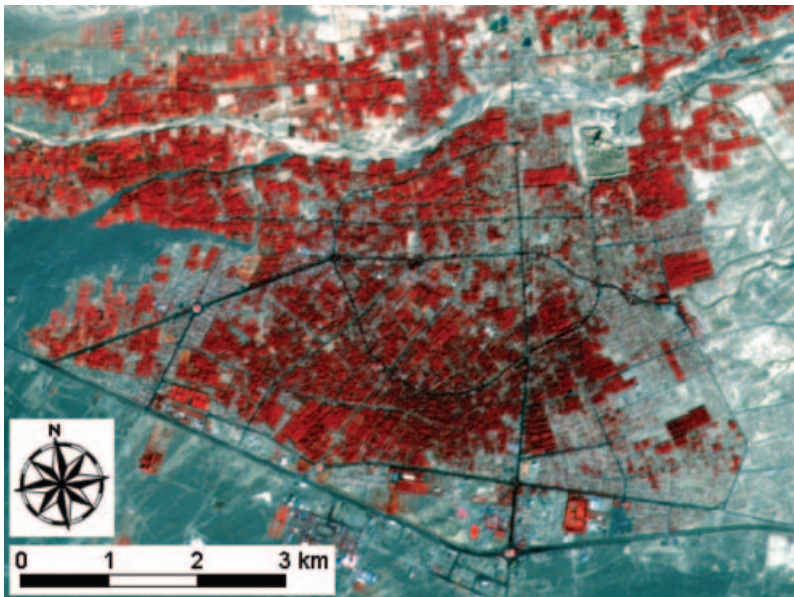

Figure 10. Post-event image of Bam City acquired on 2 January 2004; red, green and blue correspond to ASTER Bands 3, 2 and 1, respectively. The image was registered and histogram-matched from the product of radiance registered at sensor (Level 1B) to the master image.

3.3.3 Examination of the digital number fluctuation and its modelling. The means and unbiased standard deviations of DNs were calculated on a pixel-by-pixel basis. Figures 11 and 12 show the average and standard deviation of DNs of the pre-event images, respectively; those in the western areas (left in the images) were calculated from a smaller number of images than 17 due to lack of coverage as mentioned in figure 8. The characteristics of the DN fluctuations were investigated with respect to 10 sample points: five in residential areas and five on intersections of roads. These are marked in green and yellow in figure 11, respectively. Histograms of DN deviations (DN differences from the average divided by the unbiased standard deviation) of ASTER Band 1 are depicted in figures 13 and 14 with respect to the points in residential areas and those on intersections, respectively. Although the shape of the distribution of each point is not symmetric due to the limited number of pre-event images, the distribution resembles the Gaussian distribution reasonably well. The normal probability plots of the DN deviations of ASTER Band 1 are shown in figure 15. From figures 13, 14 and 15, a clear difference is not observed between the samples in residential areas and those on intersections of roads.

In figure 15, regarding Point 4, the probability of observing a value far from the median is greater than it would be for the Gaussian distribution, i.e. the distribution is heavy-tailed in a normal quantile-quantile plot with ordered data values on the vertical axis. The existence of very bright and dark objects in the fringe areas of the surrounding pixels could form this kind of distribution because the digital number of a pixel is interpolated by those of the surrounding pixels.

However, the other points do not share this heavy-tailed distribution. Thus, for simplicity, the DN fluctuation is modelled by a Gaussian distribution on a pixel-by-pixel basis with a mean and an unbiased standard deviation. It should be noted that other models such as the Student's t distribution might explain the fluctuation better for Point 4; however, strictly speaking, neither the Gaussian distribution nor the t distribution gives an exact model. This is firstly because the number of samples is too small, as suggested by small sample theory (e.g. Fisher 1970). In addition, as shown in equations (6a, b), a DN fluctuation is expressed by a weighted average of DNs of the pixels surrounding a point of interest, in which the weights are functions of the two-dimensional uniform probability distribution, and bounded by the DNs. Thus, the employed Gaussian distribution is an approximation model for simplicity. In this study, the number of pre-event images is not enough to construct a DN fluctuation model of multi-dimensional distribution of ASTER Bands 1, 2 and 3. Hence, three one-dimensional DN fluctuation models were developed and confidence levels were evaluated on a band basis based on them. The model difference among the three bands is discussed in the following section.

3.4 *Damage detection results*

The post-event image acquired on 2 January 2004 was registered and histogram-matched in the same manner as the pre-event images. Then, based on the derived stochastic models of DN fluctuation, the confidence levels, $1-\alpha(x, y)$, were evaluated for the post-event image on a pixel-by-pixel basis as follows:

$$1-\alpha(x, y) = 1 - 2\Phi\left(-\left|\frac{Q_{\text{post}}(x, y) - \mu(x, y)}{\sigma(x, y)}\right|\right) \qquad (10)$$

where $\Phi(\cdot)$ is a normal distribution function, and $Q_{\text{post}}(x, y)$, $\mu(x, y)$ and $\sigma(x, y)$ are
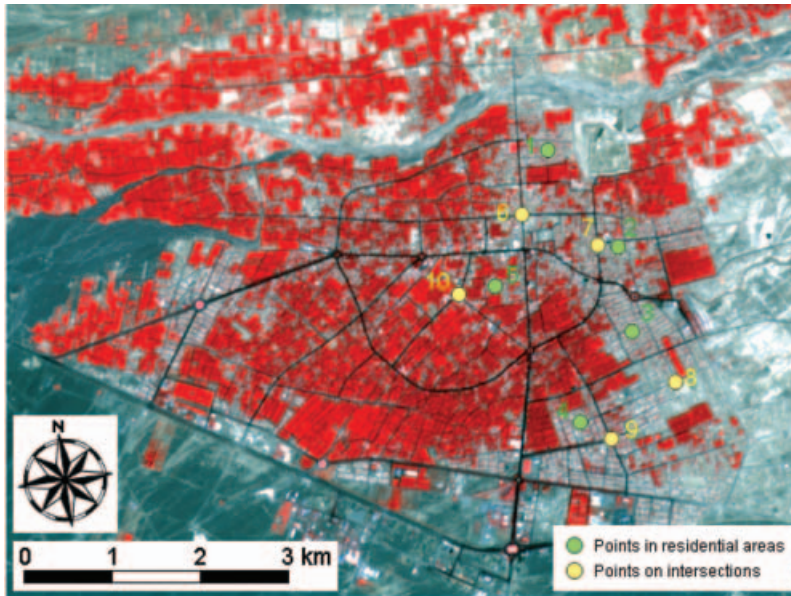
Figure 11. Average of the pre-event images of Bam City; red, green and blue correspond to ASTER Bands 3, 2 and 1, respectively. Markers show the sample points, which are used to depict histograms of digital number deviation.
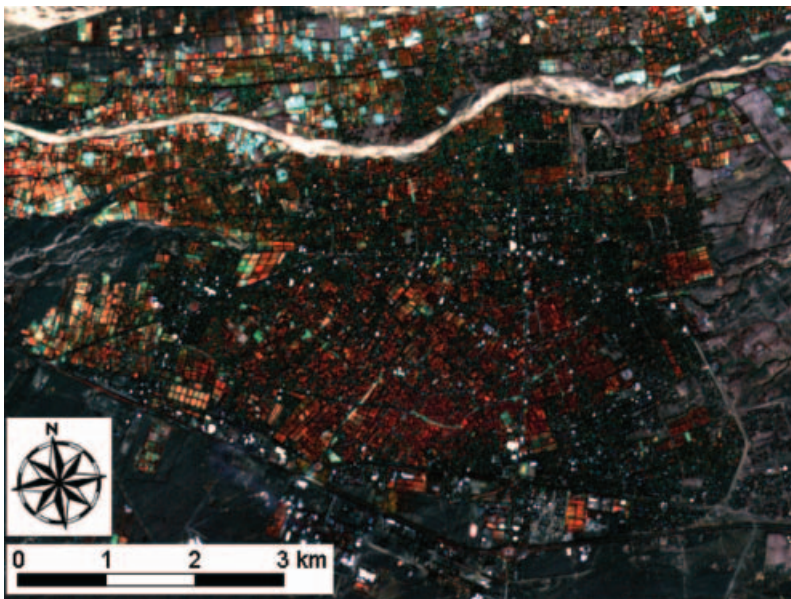

Figure 12. Standard deviation of the pre-event images of Bam City; red, green and blue correspond to ASTER Bands 3, 2 and 1, respectively.

the DN at the pixel location (x, y) in the post-event image, the mean and the standard deviation of the pre-event images at the pixel location (x, y), respectively.

Figure 16 shows the distribution of the confidence levels with respect to ASTER Band 1 of the post-event image, in which confidence levels are shown in colour on
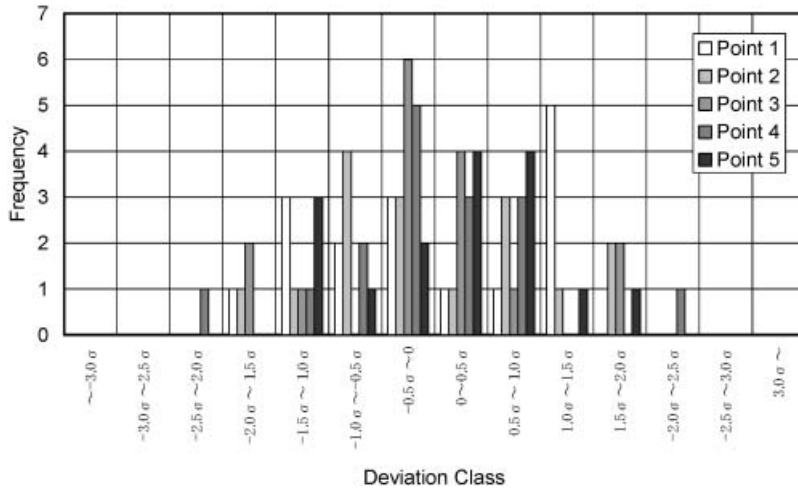
Figure 13. Histograms of digital number deviations of ASTER Band 1 with respect to the five sample points in residential areas. Unbiased standard deviations are used to form class values.
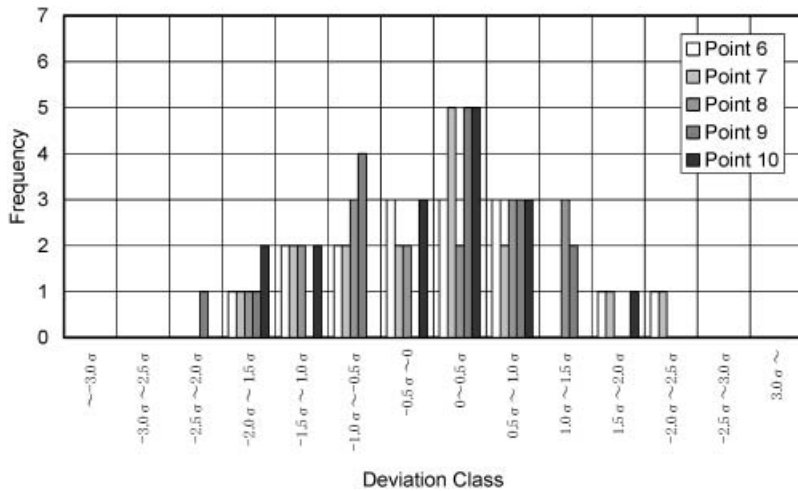

Figure 14. Histograms of digital number deviations of ASTER Band 1 with respect to the five sample points on road intersections. Unbiased standard deviations are used to form class values.

the monochrome master image of ASTER Band 1. High confidence levels, such as those shown in yellow, orange or red, suggest significant ground surface change, which appear more in the eastern part of the city. Because confidence levels reflect scaled DN change from the average in terms of the assumed Gaussian distributions, some of the confidence levels are extremely large near unity, e.g. 99.99% or greater.

For comparison, figure 17 shows the distribution of the confidence levels in the pre-event image of 28 October 2003, corresponding to no earthquake damage (but very minor change could exist due to a non-disaster event, e.g. newly constructed buildings). In this case, stochastic models were evaluated by using the 16 pre-event
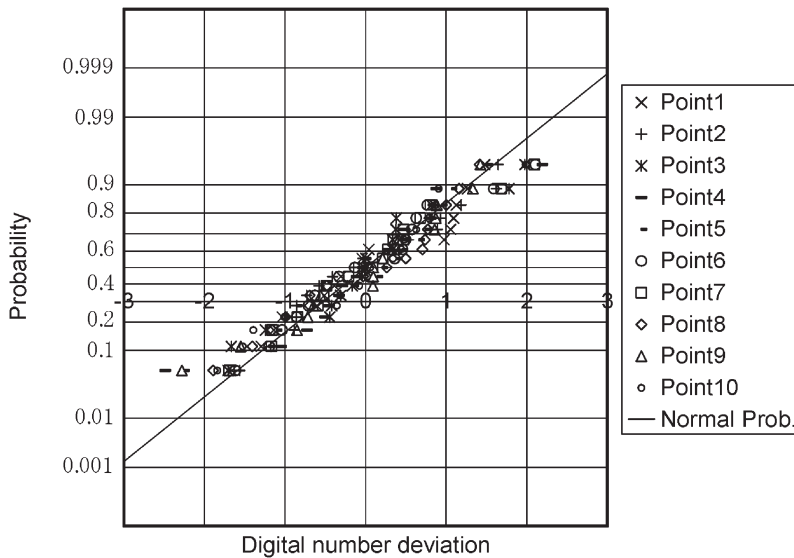
Figure 15. Normal probability plot of the digital number deviations of ASTER Band 1 with respect to 10 sample points.

images acquired before 28 October 2003. In figures 16 and 17, areas with high confidence levels in the north (upper and slightly left) of the figure are due to traces of water flow. The number of pixels with high confidence levels in figure 17 is considerably smaller than that in figure 16. This fact suggests that the proposed method may yield few commission errors (detection of false damage in non-damaged areas). In the next section the damage detection result is compared with those based on visual inspection of high-resolution images.

3.5 Comparison with the results based on high-resolution images

3.5.1 Comparison with the district-level image interpretation results. After the Bam earthquake, several organizations assessed the damage based on high-resolution satellite images or aerial photographs and made the district-level results available through the Internet (National Cartographic Center of Iran 2004, German Remote Sensing Data Center of the German Aerospace Center 2004, UNOSAT 2004, Bessis 2004). The confidence level map based on Terra-ASTER imagery was compared with these damage detection results based on high-resolution images.

The German Remote Sensing Data Center of the German Aerospace Center (2004) evaluated the damage based on the IKONOS image acquired on 27 December 2003 (Space Imaging 2004), for which resolution is 1 m in the panchromatic band and 4 m in the multi-spectral bands. Severely damaged areas were identified in the north-eastern and south-eastern parts of the city. The National Cartographic Center of Iran (2004) and United States Agency for International Development (2004) assessed the earthquake damage of Bam City based on aerial photographs and created a damage distribution map as a preliminary result. The map illustrates extensive damage in the north-eastern and south-eastern parts of the city (80–100% destroyed areas). The French sector, Service Régional de Traitement d'Image et de Télédétection (SERTIT), analysed the damage using SPOT, IRS and
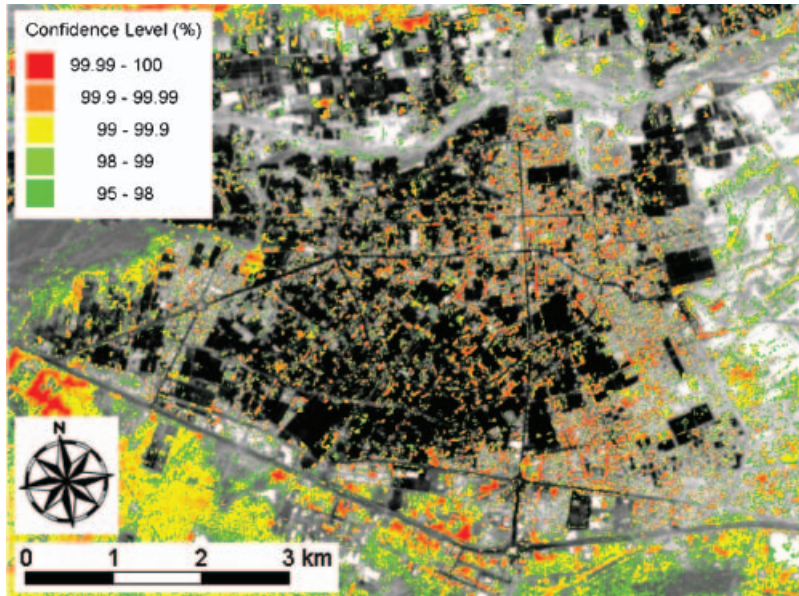
Figure 16. Distribution of the confidence levels with respect to ASTER Band 1 of the post-event image of Bam City acquired on 2 January 2004 (in colour) overlaying the monochrome master image. High confidence levels, shown in yellow, orange or red, suggest significant ground surface change, which appears more in the eastern part of the city.
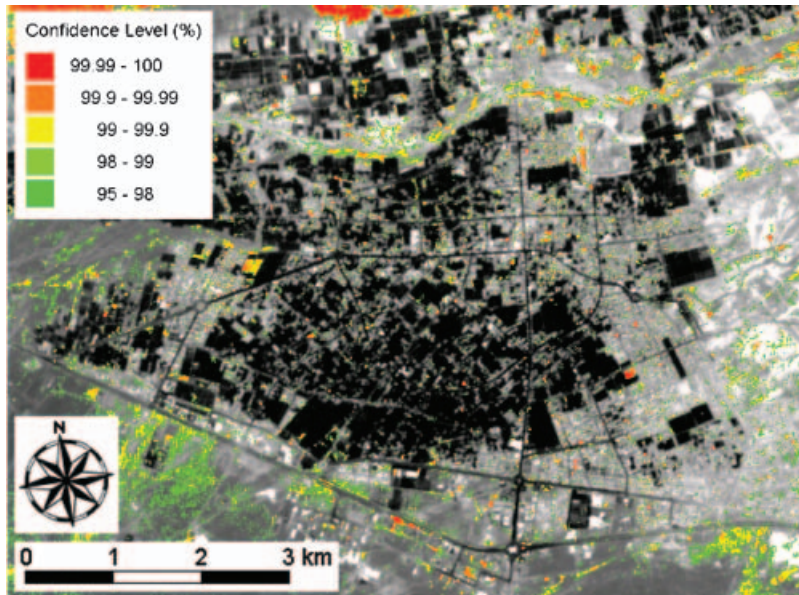

Figure 17. Distribution of the confidence level with respect to ASTER Band 1 of the pre-event image of Bam City acquired on 28 October 2003. There are considerably fewer pixels with a high confidence level in urban areas in comparison with the case using the post-event image (figure 16).

IKONOS images (UNOSAT 2004) as an activity of International Charter 'Space and Major Disasters' (Bessis 2004). The north-eastern and south-eastern parts were identified as severely damaged areas and damage was observed in the western part of the city as well. In figure 16, pixels with high confidence levels appear more in the eastern part of the city. This tendency shows agreement with these results based on high-resolution images.

3.5.2 Comparison with the result of image interpretation on a building basis. Yano *et al.* (2004) surveyed damage to buildings in Bam City based on visual inspection of the QuickBird images, for which resolution is 0.6 m in the panchromatic band and 2.4 m in the multi-spectral bands. The damage detection results derived from Terra-ASTER imagery were analysed in comparison with this visual inspection result on a building basis based on receiver operating characteristic (ROC) curves. In the damage inspection of Yano *et al.* (2004), two images were used: the pre-event image acquired on 30 September 2003 and the post-event acquired on 3 January 2004. The building damage was classified according to the European Macroseismic Scale 1998 (European Seismological Commission 1998): Grade 1, negligible to slight damage; Grade 2, moderate damage; Grade 3, substantial to heavy damage; Grade 4, very heavy damage; and Grade 5, destruction. Grade 1 and 2 damage was indistinguishable (total 1593 buildings) because sides of buildings were not observed in the satellite images, and buildings surrounded by debris (total 3790), partially collapsed buildings (total 1694) and totally collapsed buildings (total 4930) were identified as Grades 3, 4 and 5, respectively. Figure 18 shows the location of the buildings and their damage grade with colour overlaying the monochrome master image of ASTER Band 1.
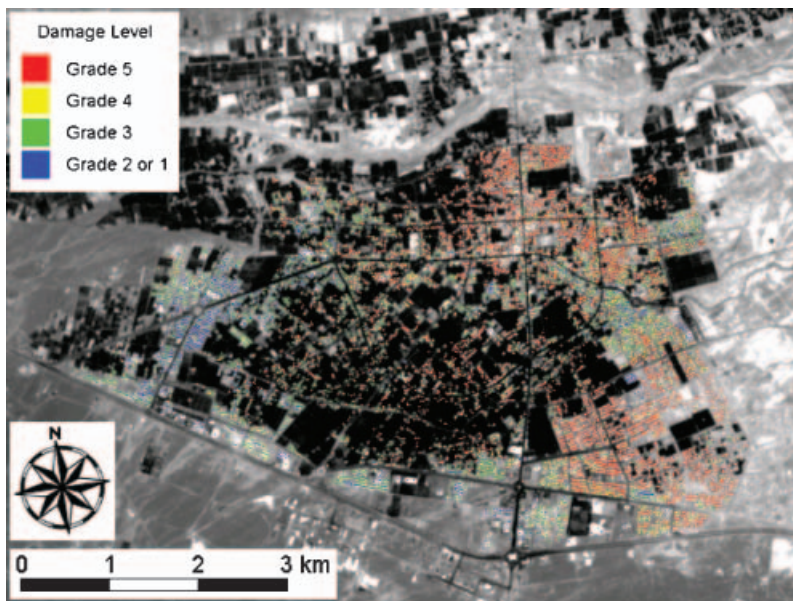

Figure 18. Visual inspection result of building damage in Bam City (in colour) based on QuickBird images acquired on 30 September 2003 and 3 January 2004 (Yano *et al.* 2004). Damage levels are based on the European Macroseismic Scale 1998 (European Seismological Commission 1998): Grade 1, negligible to slight damage; Grade 2, moderate damage; Grade 3, substantial to heavy damage; Grade 4, very heavy damage; Grade 5, destruction.

The damage classification results were stored as point data in a geographical information system, associated with the centre of buildings in the pre-event QuickBird image. First, these point locations were transformed into the coordinates of the master image of the pre-event ASTER image. Then, considering the size of buildings, the pixels within 10 m of each of the transformed points were identified and the maximum confidence level of these pixels was selected as the confidence level corresponding to the visual inspection result (Grades 1/2, 3, 4 or 5). This was in order to detect partial damage to a building and debris spread around a building. Because it was very rare for a pixel to include a whole building, visible damage most probably existed in a pixel adjoining the pixel in the centre of a building. Hence, if only the centre pixel was checked, the rate of miss (false negative) tended to increase. The radius, 10 m, was determined based on the typical size of the houses in the QuickBird image.

The ROC curve is a two-dimensional graph of probability of detection, P_D, versus the probability of false alarm, P_{FA} (Van Trees 1968, Swet and Pickett 1982, Poor 1994, Helstrom 1995, Hippenstiel 2002, Wickens 2002). In the $P_D P_{FA}$-plane, an ROC curve connects (0, 0) and (1, 1) in the upper-left-hand plane above the diagonal from (0, 0) to (1, 1). The diagonal corresponds to no detection ability, and a curve passing closer to (0, 1) means higher detection performance, i.e. the detection method has a higher signal-to-noise ratio.

The ROC curves were evaluated for each band. With respect to damage grade, three thresholds were used in order to investigate whether the detection performance changes depending on the threshold; three cases of damage occurrence were considered: Grade 3, 4 or 5/Grade 4 or 5/Grade 5. First, a certain value was assigned to the threshold of the confidence level (referred to as a cut-off value). Then, for each building, the confidence level was compared with the cut-off value and the signal was given as *positive* (the confidence level is larger than the cut-off value) or *negative* (vice versa). After that, the signal was compared with the damage occurrence and the result was classified into four categories: *true positive* (*TP*), *false positive* (*FP*), *false negative* (*FN*) and *true negative* (*TN*). The probability of detection (sensitivity or true positive rate), P_D, and the probability of false alarm (false positive rate), P_{FA}, was calculated by $P_D = TP/(TP + FN)$ and $P_{FA} = FP/(FP + TN)$, respectively, where *TP*, *FP*, *FN* and *TN* reflect the number of the above-mentioned four cases. Finally, by sliding the cut-off value, multiple points (P_{FA}, P_D) were evaluated to draw the ROC curve. Figure 19(*a*) shows the ROC curves for damage detection results based on the IFM method using Terra-ASTER images. With respect to ASTER Bands, Bands 1 and 3 show better performance than Band 2. Regarding damage grade, detection performance decreases when Grade 3 is included in the condition of damage occurrence. In order to compare ROC curves of the IFM method with those of conventional change detection methods, damage detection was conducted by temporal image differencing (TID) and temporal image ratioing (TIR). In the case of the TID method, DN difference between the post-event and pre-event images, $|Q_{post} - Q_{pre}|$, where Q_{pre} and Q_{post} are DNs of the pre-event 2003-02-27 and post-event 2004-01-02 images respectively, was used instead of confidence level in the evaluation of the ROC curves, as shown in figure 19(*b*). In the case of the TIR method, $|Q_{post} - Q_{pre}|/Q_{pre}$ was used instead of the confidence level and the ROC curves are shown in figure 19(*c*). Clearly, the ROC curves of the IFM method pass closer to the upper-left corner point than those of TID or TIR, and thus exhibit better detection performance. This is because in the IFM method a
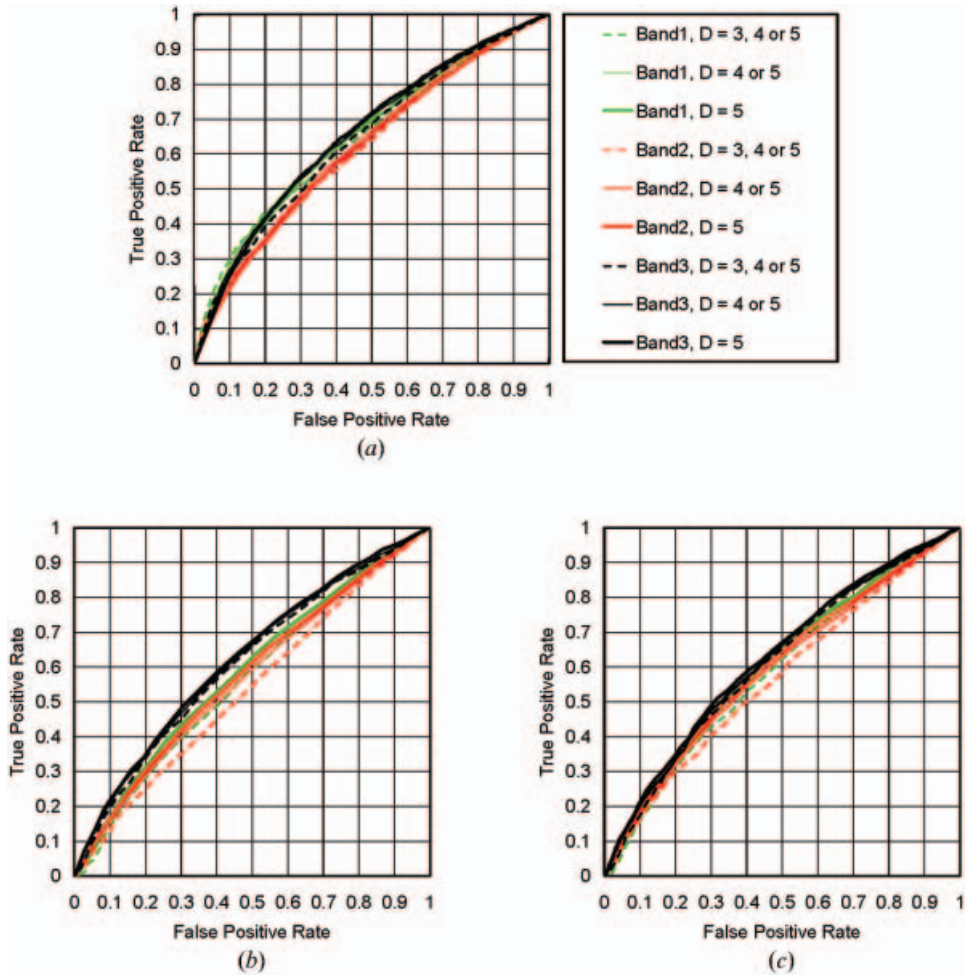
Figure 19. Receiver operating characteristic (ROC) curves for damage detection results using Terra-ASTER images based on (*a*) the Image Fluctuation Model method, (*b*) the temporal image differencing method and (*c*) the temporal image ratioing method. Nine curves in each graph were evaluated for three bands (ASTER Bands 1, 2 and 3) and three grades of damage occurrence (Grade 3, 4 or 5/Grade 4 or 5/Grade 5).

threshold (confidence level) corresponds to various DNs, which are different from pixel to pixel, while in the TID and TIR methods a threshold (DN difference or DN ratio) is uniformly applied to all the pixels in an image.

However, the detection performance of the IFM method cannot be considered good in an engineering sense: 50% or more true positive rate is desired for the region in which the false positive rate is 10% or more. The confidence level map was compared with the post-event QuickBird image (figure 20) and the causes of the low detection performance of the building damage were identified as follows: (1) Some pixels of the ASTER image included multiple buildings that had different damage levels, and these were indistinguishable due to the resolution limitation. (2) Some buildings in the residential area reflect very similar spectra and intensities even after experiencing collapse or severe damage. (3) The dusty roads were identified as
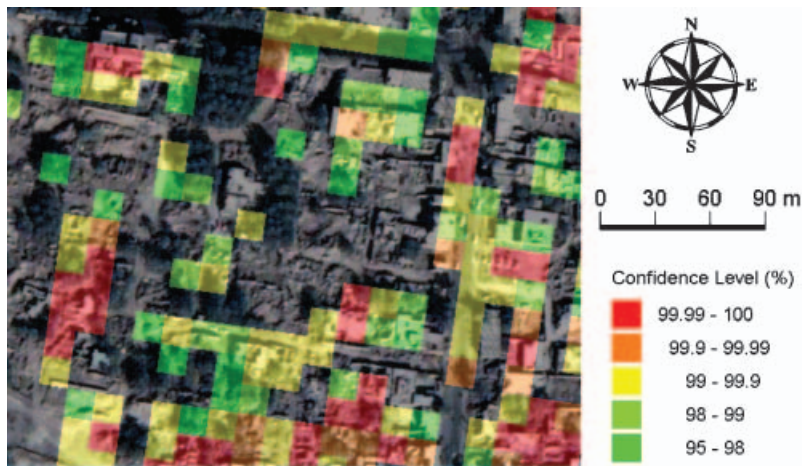
Figure 20.   Comparison between the post-event QuickBird image and the confidence level map based on the Image Fluctuation Model Method using Terra-ASTER images.

significant DN change (mostly increase), possibly due to debris spread or the demolition work. (4) Vehicles near a building were sometimes identified as significant DN change. Consequently, for more accurate damage detection in this city, texture or object-based analysis using high-resolution images, in which shapes of buildings, roads and vehicles are easily identified, might be necessary.

As far as the IFM method with the DN fluctuation model derived from multi-temporal images is concerned, the spatial resolution of Terra-ASTER is not sufficient to identify the damage experienced by each building. Rather, it reflects the general ground surface change related to a disaster event. Nevertheless, the method might be useful for detection of other damage or ground surface changes due to a hazard, such as liquefaction, flooding, wildfire, and spread of a certain material.

4.   Conclusions

A new damage (change) detection method, the Image Fluctuation Model (IFM) method using middle-resolution images acquired by satellite sensors, was proposed, which employs the probability distribution model of DN fluctuation in a normal condition and its significance test. The resulting thematic map is created from the significance level to reject the null hypothesis that the pixel DN can be considered as a sample of the DN fluctuation model.

The proposed method was applied to the 2003 Bam, Iran earthquake using Terra-ASTER images. In the case study, between 13 and 17 pre-event images were used to model the DN fluctuation. Based on the comparison between confidence level maps for pre-event and post-event images, it was suggested that the method is useful in detection of significant ground surface change due to a disaster and has few commission errors. In comparison with the result of damage assessment using high-resolution images (National Cartographic Center of Iran 2004, German Remote Sensing Data Center of the German Aerospace Center 2004, UNOSAT 2004, Bessis 2004), the confidence level map based on the IFM method shows similarity at the district level. Damage detection performance was examined by ROC curves based on the result of the visual inspection of building damage conducted by Yano *et al.* (2004) using the pre-event and post-event QuickBird images. The ROC curves of the

IFM method showed better detection performance than two conventional change detection methods: temporal image differencing and temporal image ratioing. However, the detection performance of the IFM method using Terra-ASTER images was not satisfactory in an engineering sense. This was because the limited resolution of the ASTER images could not distinguish buildings with different damage levels, some of the buildings in the study area showed very similar spectra and intensities even after experiencing collapse or severe damage, and ground surface change other than building damage, such as soil or debris spread on roads and the presence of vehicles, caused significant DN change. It was suggested that texture or object-based analysis using a high resolution image might be necessary for more accurate damage detection in this city.

In future research, the validity of modelling and the accuracy of the IFM method should be examined based on other satellite images and further ground truth data of earthquake damage. In addition, DN fluctuation models of multi-band imagery using multi-dimensional probability distributions should be examined for the improvement of accuracy.

It is also necessary to devise simple and reliable methods to construct DN fluctuation models. In the case of the 2003 Bam, Iran earthquake, 13 to 17 pre-event images were available, but this number was still not sufficient to develop a multi-band fluctuation model. Disaster relief is a highly time-sensitive matter. Thus, it will be very helpful if DN fluctuation models can be constructed with a small number of pre-event images since it would reduce the processing time in damage detection, and it is often the case that the number of available pre-event images is very limited.

One of the promising ways to model DN fluctuation without many pre-event images is to use a high-resolution image. Based on equations (6a, b), it is theoretically possible to simulate the DN fluctuation if the point spread function of a sensor is known and a single image with sufficiently high resolution is available. Another approach is to introduce a bold assumption in the characteristics of fluctuation models. In order to reduce the processing time, but at the expense of the accuracy of damage estimation, Kohiyama *et al.* (2004) introduced the assumption that all the pixels have the same standard deviation of DN fluctuation, which enables fluctuation models to be evaluated from a couple of images. This kind of approach might be effective even for the images acquired by other sensors.

References
ABRAMS, M., 2000, The Advanced Spaceborne Thermal Emission and Reflection Radiometer (ASTER): data products for the high spatial resolution imager on NASA's Terra platform. *International Journal of Remote Sensing*, **21**, pp. 847–861.
BESSIS, J.-L., 2004, Use of the International Charter Space and Major Disasters for Damage Assessment. *International Archives of Photogrammetry and Remote Sensing (IAPRS)*, volume XXXV (Proceedings of the XXth ISPRS Congress in Istanbul, Turkey), part B7, paper 117, 5 pp.

DAI, X. and KHORRAM, S., 1998, The effects of image misregistraion on the accuracy of remotely sensed change detection. *IEEE Transactions on Geoscience and Remote Sensing*, **36**, pp. 1566–1577.

Earth Remote Sensing Data Analysis Center (ERSDAC), 2001, *ASTER User's Guide*, Part I: *General*, Version 3.1 (Tokyo: ERSDAC).

ESHGHI, S. and ZARE, M., 2003, Bam (SE Iran) earthquake of 26 December 2003, Mw6.5: a preliminary reconnaissance report. http://www.iiees.ac.ir/English/bam_report_english_recc. html (as of 29 December 2003).

EUROPEAN SEISMOLOGICAL COMMISSION, 1998, *European Macroseismic Scale 1998*, G. Grünthal (Ed.) (Potsdam: GeoForschungsZentrum Potsdam).

FISHER, R.A., 1970, *Statistical Methods for Research Workers*, 14th edition (Edinburgh: Oliver and Boyd).

GERMAN REMOTE SENSING DATA CENTER OF THE GERMAN AEROSPACE CENTER, 2003, Overview satellite image map of Bam City. http://www.zki.caf.dlr.de/iran_earthquake_2003_en.html (as of 12 October, 2004).

HELSTROM, C.W., 1995, *Elements of Signal Detection and Estimation* (Englewood Cliffs, NJ: PTR Prentice Hall).

HIPPENSTIEL, R.D., 2002, *Detection Theory: Applications and Digital Signal Processing* (Boca Raton, FL: CRC Press).

KAZAKOS, D. and PAPANTONI-KAZAKOS, P., 1990, *Detection and Estimation* (New York: Computer Science Press).

KEYS, R.G., 1981, Cubic convolution interpolation for digital image processing. *IEEE Transactions on Acoustics, Speech, and Signal Processing*, **29**, pp. 1153–1160.

KOHIYAMA, M., HAYASHI, H., MAKI, N., HIGASHIDA, M., KROEHL, H.W., ELVIDGE, C.D. and HOBSON, V.R., 2004, Early damaged area estimation system using DMSP-OLS night-time imagery. *International Journal of Remote Sensing*, **25**, pp. 2015–2036.

LU, D., MAUSEL, P., BRONDIZIO, E. and MORAN, E., 2004, Change detection techniques. *International Journal of Remote Sensing*, **25**, pp. 2365–2407.

MCDONOUGH, R.N. and WHALEN, A.D., 1995, *Detection of Signals in Noise*, 2nd edition (New York: Academic Press).

MORISETTE, J.T., KHORRAM, S. and MACE, T., 1999, Land-cover change detection enhanced with generalized linear models. *International Journal of Remote Sensing*, **20**, pp. 2703–2721.

National Cartographic Center of Iran, 2004, Earthquake damage map of Bam. http://www.ngdir.ir/Downloads/Downloads.asp (as of 23 March 2004).

PARK, S.K. and SCHOWENGERDT, R.A., 1983, Image reconstruction by parametric cubic convolution. *Computer Vision, Graphics and Image Processing*, **20**, pp. 258–272.

POOR, H.V., 1994, *An Introduction to Signal Detection and Estimation*, 2nd edition (New York: Springer).

SCHOWENGERDT, R.A., 1997, *Remote Sensing: Models and Methods for Image Processing*, 2nd edition (San Diego: Academic Press).

SINGH, A., 1989, Digital change detection techniques using remotely-sensed data. *International Journal of Remote Sensing*, **10**, pp. 989–1003.

SPACE IMAGING, INC, 2004, Zoom Gallery: Bam, Iran, Zoom Gallery Archive, Earthquake damage in Bam, Iran. http://www.spaceimaging.com/gallery/zoomify/bam.htm (as of 23 March 2004).

SWET, J.A. and PICKETT, R.M., 1982, *Evaluation of Diagnostic Systems: Methods from Signal Detection Theory* (New York: Academic Press).

UNITED NATIONS, OFFICE FOR THE COORDINATION OF HUMANITARIAN AFFAIRS, 2004a, Iran: earthquake OCHA situation report no. 15. http://www.reliefweb.int (as of 17 March 2004).

UNITED NATIONS, OFFICE FOR THE COORDINATION OF HUMANITARIAN AFFAIRS, 2004b, IrAN: Tehran lowers Bam earthquake toll. http://www.irinnews.org/report.asp?

ReportID=40323& SelectRegion=Central_Asia&SelectCountry=IRAN (as of 30 March 2004).

UNITED STATES AGENCY FOR INTERNATIONAL DEVELOPMENT, 2004, Iran: estimated damage caused by the Bam earthquake. http://www.reliefweb.int/w/map.nsf/wPreview/5613CC5E3F922B 6785256E1400782392 (as of 5 January 2004).

UNOSAT, 2004, Bam city overview: damages zonation map from satellites data. http://unosat.web.cern.ch/unosat/asp/prod_free.asp?id=38 (as of 12 October 2004).

VAN TREES, H.L., 1968, *Detection, Estimation, and Modulation Theory*, Part I: *Detection, Estimation, and Linear Modulation Theory* (New York: Wiley).

WICKENS, T.D., 2002, *Elementary Signal Detection Theory* (Oxford: Oxford University Press).

YAMAGUCHI, Y., KAHLE, A.B., PNIEL, M., TSU, H. and KAWAKAMI, T., 1998, Overview of Advanced Spaceborne Thermal Emission and Reflection Radiometer (ASTER). *IEEE Transactions on Geoscience and Remote Sensing*, **36**, pp. 1062–1071.

YANO, Y., YAMAZAKI, F., MATSUOKA, M. and VU, T.T., 2004, Building damage detection of the 2003 Bam, Iran earthquake using QuickBird images. In *Proceedings of the 25th Asian Conference on Remote Sensing*, 22–26 November 2004 (Bangkok: Geo-Informatics and Space Technology Development Agency), pp. 618–623.